

Sensitivity of climate simulations to radiative effects of tropical anvil structure

Charles S. Zender and J. T. Kiehl

National Center for Atmospheric Research, Boulder, Colorado

Abstract.

Climate sensitivity to the representation of tropical anvil is investigated in a version of the National Center for Atmospheric Research Community Climate Model. Common features of tropical anvil generation and structure, consistent with observations and cloud resolving models, are incorporated into a simple prognostic anvil parameterization. These features include anvil convective origin, vertical profile, phase, areal extent, and lifespan. Two numerical climate integrations are forced by 1985–1989 sea surface temperature (SST): the control, with simple diagnostic anvil, and the experiment, which simulates tropical anvil structure prognostically. The prognostic anvil formulation enhances ice and reduces liquid in the tropics. Increase in hydrometeor size associated with anvil weakens cloud radiative extinction per unit mass by factors of 1–3. The weaker mass extinction efficiency approximately balances enhanced ice amount so that anvil ice mass quadruples without biasing the mean radiative energy balance, but significantly alters the vertical distribution of radiative effects. Enhanced anvil perturbs the tropical upper troposphere temperature structure more strongly in winter, when the column is clearer and anvil radiatively heats the troposphere above 200 mb. In the summer tropics, enhanced anvil reduces radiative cooling up to 200 mb, and enhances cooling above that. The prognostic anvil formulation improves longwave cloud radiative response to SST cooling but worsens response to warming > 2 °C. The net response of convection is a shift toward the winter hemisphere in solstice months. These changes lead to a significant response in the extratropical height field in January. These results emphasize the importance of representing tropical anvil structure in climate simulations.

1. Introduction

¹Radiative forcing from the extended tropical upper tropospheric cloud known as cirrus anvil plays a dominant role in determining the diabatic heating which drives the general circulation. Tropical cirrus anvil originates in the complex interaction of a mesoscale convective system (MCS) with the environment. A general

circulation model (GCM) does not resolve this interaction and must rely on sub-gridscale methods to diagnose or predict anvil cloud. This study combines distinctive features of tropical anvil structure into a parameterization suitable for GCMs, and then examines the impact of accounting for the radiative effects of tropical anvil on the climate system.

The radiative effects of anvil depend on its distinctive lifecycle and structure, which may be briefly summarized as follows: Deep convection is the ultimate source of tropical upper tropospheric extended clouds,

¹Copyright 1997 by the American Geophysical Union.

Paper number 97JD02009
0148-0227/97/97JD-02009\$09.00

i.e., tropical anvils [e.g., *Webster and Stephens*, 1980]. The relative area of convecting cores to the associated anvil is 10–20% [*Leary and Houze*, 1980; *Fu et al.*, 1990]. Anvil lifetime, typically 6–12 hr [*Ackerman et al.*, 1988; *Leary and Houze*, 1980], exceeds the duration of deep convection by many hours [*Houze*, 1989]. Thus, although the cumulonimbus core produces the strongest radiative impact per unit area, the anvil region dominates the radiative impacts of the convective cluster as a whole [*Machado and Rossow*, 1993; *Wong et al.*, 1993b]. *Leary and Houze* [1980] and [*Gamache and Houze*, 1983] inferred the hydrologic budgets of tropical convective systems from observations: Roughly 60–75% of anvil condensate is detrained from deep convective updrafts. The remainder, roughly 25–40% of anvil mass, is generated by circulations outside the deep convective core, i.e., in the anvil itself. Roughly 40% of MCS precipitation comes from the stratiform region. Observations and numerical simulations [e.g., *Wong et al.*, 1993a; *Sui et al.*, 1994; *Grabowski et al.*, 1996; *McFarquhar and Heymsfield*, 1996, 1997] show time mean condensate mixing ratio q_c in tropical convective systems does not decrease significantly (but can increase) from the freezing level to ~ 300 mb, above which q_c decreases rapidly. The intrinsically mesoscale nature of these anvil features has hindered their representation in most GCM moist convection schemes [*Donner*, 1993]. How explicitly should these features of anvil structure and lifecycle be represented in GCMs? The answer depends on climate sensitivity to tropical anvil.

Many previous GCM studies have advanced understanding of climate sensitivity to tropical anvils by modeling climate sensitivity to anvil representation. *Ramanathan et al.* [1983] showed non-black cirrus is crucial to maintaining the observed tropical upper troposphere temperature structure and meridional temperature gradient. *Charlock and Ramanathan* [1985] showed simulated zonal average upper troposphere temperature increased significantly when treating frozen cloud particles as $20\ \mu\text{m}$ larger than liquid. *Slingo and Slingo* [1988] showed tropical anvil not only warms the tropical upper troposphere, but also accelerates the subtropical jets and excites responses in the northern hemisphere winter height field. *Ramaswamy and Ramanathan* [1989] showed shortwave heating in tropical anvil is a significant fraction of total diabatic heating above 300 mb, and plays an important role in the maintenance of the upper tropospheric temperature structure. Furthermore, they suggested the relative abundance of detached cirrus anvil to anvil embedded in deep convective systems determines the sign of net ra-

diative heating above 300 mb. *Ramanathan and Collins* [1991] hypothesized cirrus radiative forcing can be an important negative feedback for stabilizing column energy changes induced by local positive SST anomalies over warm ocean. *Senior and Mitchell* [1993] showed representing ice cloud prognostically rather than diagnostically could substantially alter modeled climate sensitivity to CO_2 doubling and SST change. *Sherwood et al.* [1994] examined climate sensitivity to anvil radiative forcing over the west Pacific warm pool. They showed atmospheric heating by tropical cirrus is primarily balanced by vertical advective cooling, in accord with *Ackerman et al.* [1988]. *Lohmann and Roeckner* [1995] showed climate response to blackbody cirrus forcing resembles the response to increased SST forcing even though the direct heating mechanisms, enhanced cirrus radiative heating and surface evaporation, respectively, are vertically distinct.

These GCM studies employed a variety of methods to determine anvil condensate amount. Most of the aforementioned studies diagnose anvil cloud from atmospheric thermodynamic properties (e.g., relative humidity, column vapor, and stability). However, prognostic schemes are more physically based than diagnostic. *Senior and Mitchell* [1993] showed radiative feedbacks from prognostic cloud could be significantly different than feedbacks from cloud diagnosed from relative humidity. Newer GCMs [e.g., *Tiedtke*, 1993; *Del Genio et al.*, 1996] prognose stratiform anvil cloud from bulk microphysics. These schemes detrain condensate predicted by the moist convection parameterization into the stratiform anvil.

Our motivation in the present study is to examine the role of tropical anvil radiative forcing in a climate where the representation of tropical anvil agrees with the gross behavior of tropical mesoscale convective systems, summarized above. We replace a representation of tropical cloud which diagnoses cloud mass from column vapor with a prognostic representation which forecasts anvil generation from the vertical profile of convective mass flux and anvil precipitation from mesoscale budget estimates. Thus, the forcing in the experiment is an integrated set of constraints (ratio of convective condensate generation to vertical mass flux profile, horizontal extent, vertical condensate profile, ice fraction, ratio of mesoscale precipitation to sublimation, and lifetime) consistent with tropical anvil structure but not present in most current GCM cloud parameterizations. By comparing the simulated climates to each other we can deduce climate sensitivity to the representation of tropical anvil structure.

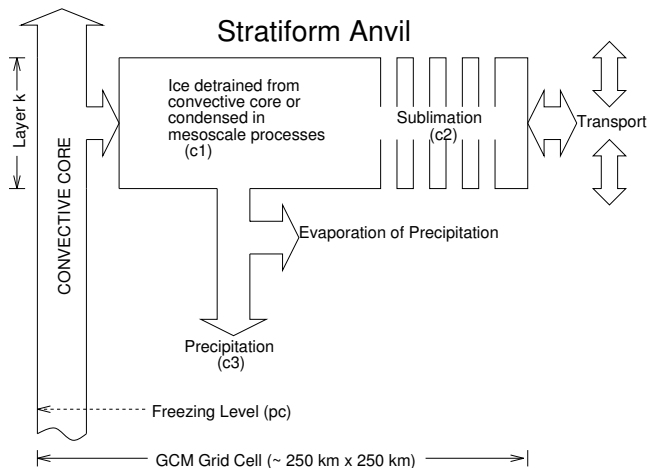


Figure 1. Conceptual model of the ice budget in ANV. c_1 – c_3 and p_c are free parameters.

The parameterization of tropical anvil used in the numerical climate experiment is developed in section 2. Section 3 presents the mean climate response to the tropical anvil representation. Section 4 examines anvil response to SST forcing in the 1987 El Niño. Section 5 contains the conclusions.

2. GCM Anvil Parameterization

Spatio-temporal scale mismatch between convective and stratiform processes and GCM resolution makes anvil parameterization difficult. GCMs currently employ two common methods to represent these processes: (i) diagnosing anvil cloud from column thermodynamic properties (e.g., relative humidity) and (ii) prognosing anvil cloud by assuming an anvil detrainment efficiency which acts on the convective mass flux predicted by the moist convection scheme. Diagnostic methods like (i) have difficulty representing convective-radiative hysteresis, such as the radiative influence of detached anvils. As *Donner* [1993] points out, prognostic methods like (ii) often do not explicitly account for the 25–40% of anvil mass formed by secondary circulations outside the deep convective core.

Cloud resolving models and mesoscale budget studies suggest the hydrologic structure of MCS anvils may be simply parameterized in terms of large scale forcing. Figure 1 shows our modified version of the *Leary and Houze* [1980] conceptual anvil model. We implement the parameterization of this conceptual anvil model, denoted ANV, as follows: For a grid cell of density ρ and ice mixing ratio q_i located in a convecting column with

convective mass flux M_c at 500 mb, the ice budget that defines ANV is:

$$\frac{Dq_i}{Dt} = \frac{c_1 M_c}{\rho \Delta Z} - c_2 q_i - c_3 q_i \quad (1)$$

where ΔZ is the thickness of the convecting portion of the column in which $T < 0^\circ\text{C}$. q_i , ρ , and the wind vector \vec{u} (hidden in the material derivative) vary in the vertical. The material derivative on the LHS accounts for advection. In this study the advection of the prognostic ice is computed using the same semi-Lagrangian advection algorithm used for water vapor *Williamson and Rasch* [1994]. The first term on the RHS relates the generation of total column ice to M_c . Basing the generation of q_i throughout the anvil on the mass flux near anvil base M_c (rather than local M) produces a vertical profile of q_i which increases or remains constant (rather than significantly decreasing) from anvil base up to ~ 300 mb, in accord with current understanding [e.g., *Houze*, 1989; *Wong et al.*, 1993a]. Justification for the c_1 term is described in the next section. The c_2 term represents local sublimation of the anvil due to sub-gridscale entrainment and subsaturation. The c_3 term converts ice to precipitation.

Parameters c_1 – c_3 do not vary in time or space—they are the free parameters of the parameterization. The values of c_1 – c_3 which yield a realistic climate depend on the physical parameterizations (e.g., moist convection) used in the host GCM. c_2 and c_3 are determined from observations [*Leary and Houze*, 1980; *Gamache and Houze*, 1983] and process studies in a microphysical cloud model [*Zender and Kiehl*, 1994]. The present study sets $c_1 = .75 \times 10^{-3}$, $c_2 = .3c_3$, and $c_3 = 1.85 \times 10^{-4} \text{ s}^{-1}$. We assume the detrained anvil completely covers a gridcell, i.e., cloud fraction is 1. At the GCM scale (i.e., horizontal gridscale > 100 km), this assumption overestimates anvil coverage relative to observations *Leary and Houze* [1980]; *Houze* [1989]; *Mapes and Houze* [1993].

2.1. Linking Anvil Growth to Anvil-base Mass Flux

Prior studies indicate convective mass flux M is the best single parameter to characterize the formation of tropical anvil. *Xu and Krueger* [1991] concluded M best predicts tropical convective cloud amount and the ice water content of individual anvil layers. Based on satellite observations, *Machado and Rossow* [1993] suggested convective mass flux at the base of cumulonimbus cores determines the mean cloud properties of mesoscale convective systems, including the stratiform anvil region.

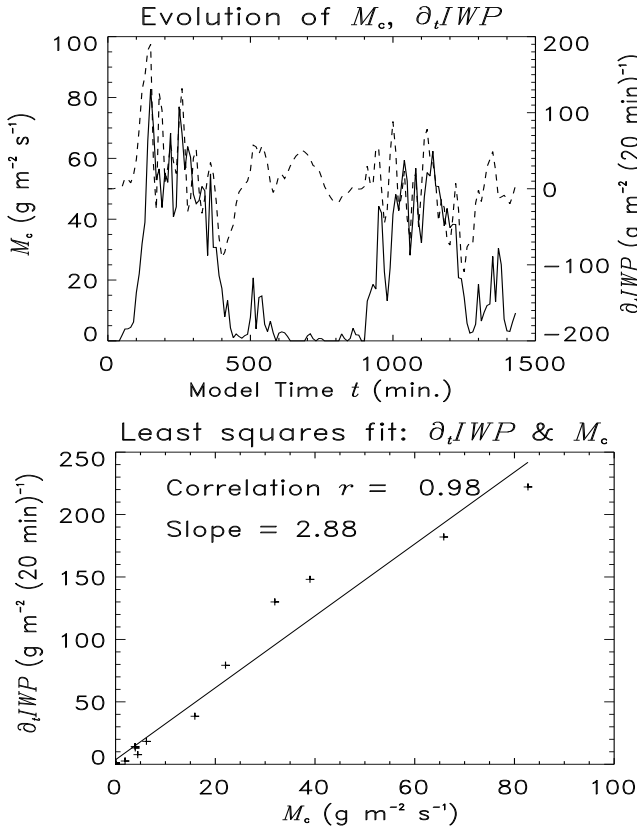


Figure 2. Results of Cumulus Ensemble Model experiment. (a) Evolution of 500 mb convective mass flux M_c (g m^{-2}) (solid) and IWP (dashed) during the first 24 hours of the CEM simulation. IWP is expressed in $\text{g m}^{-2} (20 \text{ min})^{-1}$, i.e., mass change per GCM timestep. (b) Linear correlation and least squares fit of 500 mb convective mass flux M_c ($\text{g m}^{-2} \text{s}^{-1}$) to anvil growth rate IWP ($\text{g m}^{-2} (20 \text{ min})^{-1}$) from the the first 2.5 hours of (a).

We use a cloud resolving, cumulus ensemble model (CEM) to provide a high spatial and temporal resolution dataset which spans the range of MCS activity from the convective to the GCM scale. A comprehensive review of our CEM simulation is presented by *Grabowski et al.* [1996]. Figure 2a shows the variation of M_c and anvil mass growth rate IWP through the first day of the CEM simulation. The initial anvil formation, lasting about six hours, occurred as a prescribed thermal instability triggered concentrated convective updrafts (cores) which detrained frozen condensate into a cirrus anvil above 500 mb. The variation of IWP is strongest during convectively active periods, and subdued during

the convectively quiescent period ($400 < t < 900 \text{ min}$) between the first and second generation anvils. Non-convective formation of anvil ice is also evident during the quiescent period. Periods when IWP is negative occur when net anvil dissipation (due to precipitation and sublimation) exceeds production.

In order to isolate the processes controlling ice generation from destruction we focused on the initial hours of anvil formation, when a single convective tower dominated the mass budget of the entire domain. Figure 2b shows the correlation of M_c and IWP through the first 2.5 hr of the CEM simulation. This initial correlation is excellent, but anvil decay processes and scattered convection within the CEM domain cause the correlation to deteriorate after 2.5 hr. The slope of the least squares fit between M_c and IWP provides the initial estimate for c_1 in (1). Note IWP includes convectively detrained condensate as well as condensate produced in the young anvil. The parameter c_1 is intended to implicitly account for the anvil mass formed by both convective and mesoscale circulations. The results of our GCM simulations with constant c_1 (below) show numerous improvements in anvil climatology over a more traditional method. Parameterizing c_1 from an ensemble of CEM integrations, perhaps as a function of large scale forcing (e.g., wind shear, SST) is the next logical step.

2.2. Ice Fraction and Hydrometeor Size

Recent field observations and models [e.g., *Sui et al.*, 1994; *Grabowski et al.*, 1996; *Gregory and Morris*, 1996] suggest that, above 500 mb, anvil condensate is dominated by ice. In terms of temperature, the complete phase transition may occur over less than 10°K . The control model, a version of the National Center for Atmospheric Research Community Climate Model [*Kiehl et al.*, 1996] denoted CCM, partitions diagnostic condensate between liquid and ice via

$$f_i^{\text{CCM}} = \begin{cases} 0 & T > -10^\circ \text{C} \\ -\frac{T+10}{20} & -10 \geq T \geq -30^\circ \text{C} \\ 1 & T < -30^\circ \text{C} \end{cases} \quad (2)$$

The experiment, denoted ANV, restricts diagnostic liquid condensate (and, hence, mixed phase cloud) to a narrower and warmer range than the control model according to

$$f_i^{\text{ANV}} = \begin{cases} 0 & T > 0^\circ \text{C} \\ -\frac{T}{5} & 0 \geq T \geq -5^\circ \text{C} \\ 1 & T < -5^\circ \text{C} \end{cases} \quad (3)$$

Since CCM classifies some condensate as cold as -30°C as liquid (2), while ANV has no liquid colder than -5°C

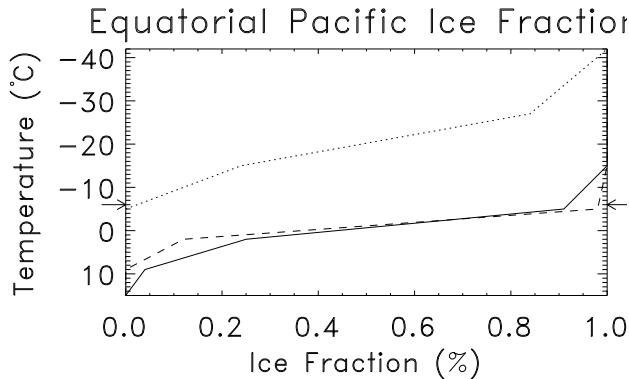


Figure 3. Modeled ice fraction f_i over the equatorial Pacific in July for the CEM (solid), CCM (dotted), and ANV (dashed). Arrows indicate 500 mb level.

(3), it is clear the ANV atmosphere will contain much more ice than the CCM. The effect of using (2) vs. (3) is shown in Figure 3, which shows the vertical distribution of f_i averaged over the equatorial Pacific (140–270 °E, 10 °S–10 °N) for each GCM layer in the mixed phase region (GCM data are from the simulations described below). ANV underestimates liquid condensate near 500 mb but otherwise agrees with the CEM ((3) imposes the agreement). CCM cloud has the same mixed phase composition as ANV cloud approximately 20 °C warmer.

For both the control and the experiment, the determination of hydrometeor size and its radiative treatment is as described in *Kiehl et al.* [1996]: Model cloud droplet effective radius r_{el} is fixed at 10 μm over ocean and sea ice but varies from 5–10 μm over land. Ice crystal effective radius r_{ei} represents an equivalent surface area sphere and varies linearly with a normalized pressure coordinate. Over ocean this results in $r_{ei} = 10 \mu\text{m}$ for $p > 800$ mb to $r_{ei} = 30 \mu\text{m}$ for $p < 400$ mb. Solar single scattering and longwave emissivity properties are from *Slingo* [1989] (liquid) and *Ebert and Curry* [1992] (ice).

Since ice hydrometeors are prescribed to be larger than liquid, classifying more condensate as ice (3) also decreases the extinction efficiency per unit mass of anvil [e.g., *Zender and Kiehl*, 1994]. This proves to be an important factor in diagnosing the cause of change in climatological cloud radiative properties in this sensitivity study.

2.3. Diagnostic Condensate Formation

For convenience, this section summarizes the diagnostic treatment of condensate employed in the control model, CCM. For a fuller description, the reader is referred to *Kiehl et al.* [1996]. In CCM, grid box average q_c is logarithmically proportional to total column vapor Q_v and linearly proportional to local cloud fraction A through

$$q_c = A\rho_\ell/\rho \quad (4)$$

$$\rho_\ell = \rho_\ell^0 e^{(-z/h_\ell)} \quad (5)$$

$$h_\ell = 810 \ln Q_v \quad (6)$$

where ρ is density, $\rho_\ell^0 \equiv .18 \text{ g m}^{-3}$ is “in-cloud” condensed water density at the surface, z is height, and h_ℓ is the scale height of condensed water. Note the strong coupling of q_c to local surface temperature by the Clausius-Clapeyron relationship implicit in (6). Inserting tropical values for Q_v we find $h_\ell \lesssim 4$ km so that q_c monotonically decreases from the surface (for fixed A). A drawback to this procedure is that the upper tropospheric peak in q_c profile of an anvil system must be captured by significantly modulating A across the anvil deck (4).

3. Sensitivity Study Results

To assess climate sensitivity to the features of convectively generated anvil described above, we compare the results of two numerical climate integrations forced with observed 1985–1989 SST. The control, denoted CCM, uses a diagnostic cloud scheme with no special provisions for anvil [*Kiehl et al.*, 1996]. The experiment, denoted ANV, forecasts anvil ice from (1), which incorporates modeled and observed characteristics of tropical anvil production and structure (i.e., explicitly linking anvil condensate generation to anvil base convective mass flux, strong vertical profiles of condensate up to 300 mb, and increased ice fraction). The focus of the present study is on the radiative effects of the anvil condensate. Thus we restrict the effects of q_i in (1) to radiative heating alone. The results focus on tropical climate, where anvil forcing is greatest.

3.1. Condensate Distribution

The climate response to anvil representation is driven by radiative forcing resulting from the distribution, partitioning (ice or liquid), and size of cloud condensate. The direct effect of representing the structure and convective production of anvils is to sequester more condensate in the upper troposphere, a larger fraction

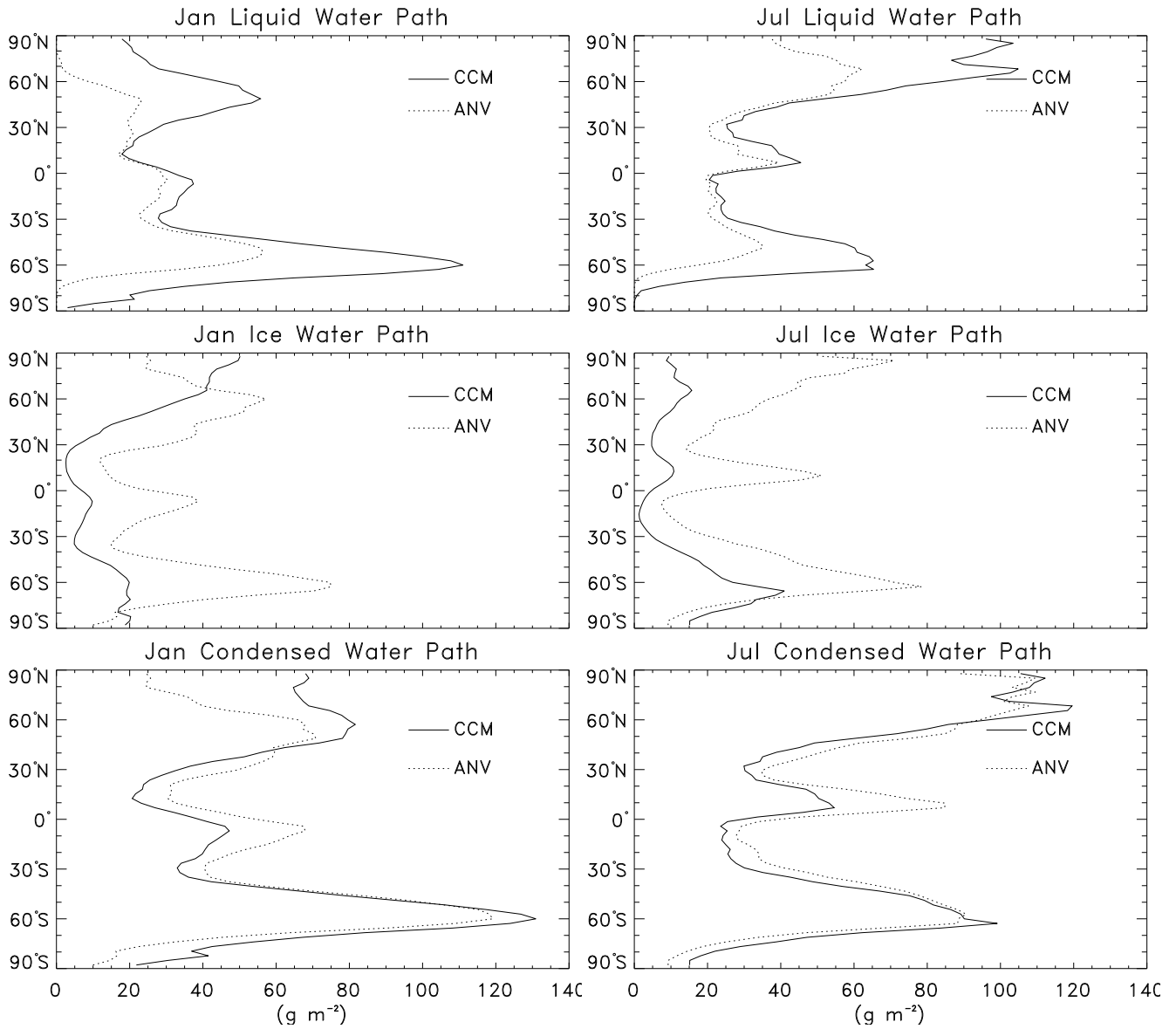


Figure 4. Zonal average column condensate burdens (g m^{-2}) from 1985–1989 (left) January and (right) July simulations by (solid) CCM and (dashed) ANV of (a,b) LWP, (c,d) IWP, and (e,f) CWP.

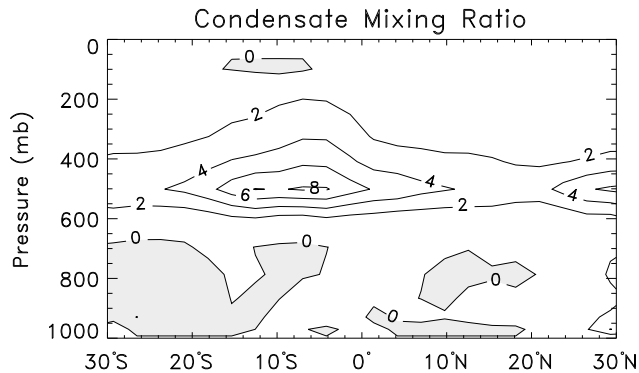


Figure 5. Change (ANV–CCM) in zonal average condensate mixing ratio q_c (mg kg^{-1}) due to prognostic anvil representation. Contour interval is 2 mg kg^{-1} . Shading indicates values < 0 . Data are from ensemble averages of 5 simulated Januarys from 1985–1989.

of which is ice. Figure 4 separates modeled January and July total condensed water path CWP by phase ($\text{CWP} \equiv \text{LWP} + \text{IWP}$). The refined anvil representation increases tropical IWP by factors of 2–4, and reduces tropical LWP by 20%. The net increase in tropical CWP is 10–50%, comprising a mean increase of upper tropospheric condensate with a repartitioning of condensate from liquid to ice due to (3). The mean increase is partly due to implicitly accounting for anvil formed in mesoscale circulations. The tropical response to the experiment in July is similar to January in the preponderance of the results. Thus for economy we omit showing July results in most of the following fields.

Figure 5 contours the ensemble mean January vertical profile of change in zonal average condensate q_c in the tropics. The largest model differences occur in the ascending branch of the Hadley cell, where the 600–200 mb maxima signals enhanced tropical anvils with better vertical definition. These changes in condensate distribution and ice fraction (2–3) agree with inferences from recent observations [Wong *et al.*, 1993a; Gregory and Morris, 1996; McFarquhar and Heymsfield, 1996, 1997] and cumulus ensemble model simulations [Sui *et al.*, 1994; Grabowski *et al.*, 1996].

Before examining the climate response to changes in anvil structure, it is of interest to estimate the relative roles of the two major modifications to the original CCM anvil treatment in forcing the climate. To describe this relative forcing, we examine the terms in the

linearized net TOA energy budget,

$$\Delta F = \frac{\partial F}{\partial \text{CWP}} \Delta \text{CWP} + \frac{\partial F}{\partial f_i} \Delta f_i + \dots \quad (7)$$

where F represents a net radiative flux and Δ the change between the control and the experiment. Thus the LHS is the net radiative climate response to the forcings on the RHS. The first term on the RHS represents the climate forcing due to the radiative effects of the change in condensate path CWP and vertical location which arise from the prognostic formulation of anvil generation (1) (cf. Figure 5). The second term on the RHS represents the climate forcing due to the radiative effects of the increase in ice fraction f_i arising from (3) (cf. Figure 3). These two terms are the dominant forcing mechanisms in the experiment. The global annual average TOA radiative budgets of the control and the experiment balance to within $.5 \text{ W m}^{-2}$, agree between models to within 2.5 W m^{-2} (agreement with ERBE is within 4 W m^{-2}). In other words $\Delta F \approx 0 \text{ W m}^{-2}$ for F representing TOA flux or cloud forcing. In particular, the zonal average TOA radiative budgets of the models closely agree in the tropics. The agreement holds for the total radiative fluxes and the shortwave and longwave components separately (the surface energy budgets are similarly balanced).

The sensitivity factors in (7) were estimated with an offline, column version of the CCM radiation code. We obtained $\partial F / \partial \text{CWP}$ by differencing the diurnal average radiative fluxes from the control and experimental zonal average q_c profiles for January at 5°S , using the CCM ice fraction (2) for both profiles. Similarly, $\partial F / \partial f_i$ was estimated by differencing the fluxes obtained using the control and experimental ice fractions on the CCM q_c profile. From these computations, the prognostic formulation for anvil structure alone (1) imposes a -19 W m^{-2} shortwave forcing and a $+24 \text{ W m}^{-2}$ longwave forcing in the tropics, for a net radiative forcing of $+5 \text{ W m}^{-2}$. Thus the increased upper tropospheric condensate due to (1) and shown in Figures 4 and 5 acts to significantly strengthen tropical cloud radiative forcing. The enhanced ice fraction alone (3) imposes a $+10 \text{ W m}^{-2}$ shortwave forcing and a -9 W m^{-2} longwave forcing in the tropics, for a net radiative forcing of $+1 \text{ W m}^{-2}$. Thus the increased upper tropospheric ice fraction due to (2) and shown in Figures 3 and 4 acts to significantly weaken tropical cloud radiative forcing. As mentioned in Section 2.2, this is largely due to the larger hydrometeor size associated with ice. The magnitude of the tropical radiative forcing by the increased upper tropospheric condensate is 2–3 times the magnitude of the forcing due to the increased ice fraction.

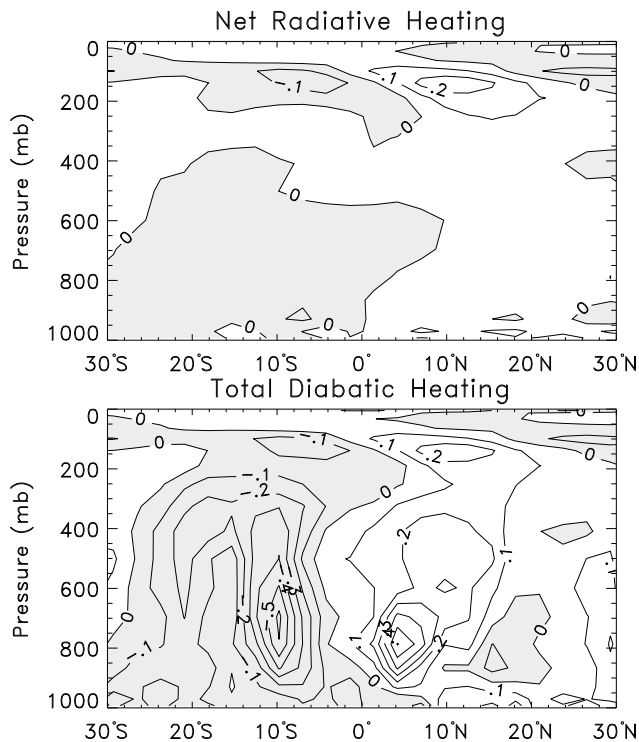


Figure 6. As in Figure 5 but for (a) radiative heating Q_R only, and (b) total diabatic heating Q_T . Contour intervals are $.1 \text{ K day}^{-1}$.

3.2. Tropical Upper Tropospheric Heating

In this experiment the changes in tropical anvil structure force the circulation by altering total radiative heating Q_R . Anvil induced changes in the vertical and horizontal distribution of Q_R alter total diabatic heating Q_T , which includes latent heating (Q_L), radiation (Q_R), and diffusion (turbulence). Figure 6 shows the change in zonal average Q_R and Q_T in the tropics. Changes above 200 mb, where condensation is weak, are due to the radiative heating perturbation induced by the enhanced anvil. Enhanced anvil perturbs tropical upper troposphere heating more strongly in winter, when the column is clearer and anvil radiatively heats the troposphere above 200 mb. In the summer tropics, enhanced anvil occurs in a cloudier environment, reducing radiative cooling up to 200 mb, and enhancing cooling above that. Thus, winter and summer tropics fall, respectively, into the “anvil” and “deep” cloud scenarios of *Ramaswamy and Ramanathan [1989]*. Reduced optical depth keeps the intrinsically greater solar absorption of ice (relative to liquid) from causing a

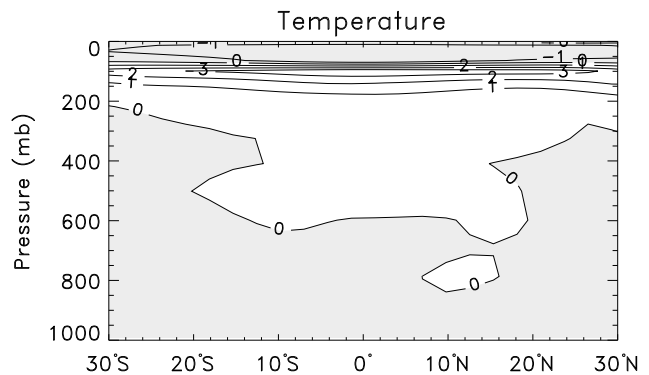


Figure 7. As in Figure 5 but for temperature T ($^{\circ}\text{K}$). Contour interval is $.1 \text{ }^{\circ}\text{K}$.

ubiquitous heating increase above 600 mb.

Beneath 200 mb, change in Q_T is dominated by change in latent heating Q_L . The response in Q_L is, to first order, induced by the change in Q_R . Convection intensifies from $0\text{--}10^{\circ}\text{N}$ in ANV in both seasons, reflecting an enhanced ITCZ, notably over Micronesia, the east Indian Ocean, and northeast of Brazil. Deep convection in the remainder of the ascending branch of the Hadley circulation is reduced. Weaker summer hemisphere diabatic heating in ANV reduced Hadley cell strength by 13% in January, 7% in July. Change in tropical water vapor (not shown) strongly resembles ΔQ_L .

Figure 7 shows ANV warms the 50 mb beneath the tropical tropopause by $2\text{--}3 \text{ }^{\circ}\text{K}$, roughly 5 times the standard deviation of zonal average monthly T from a 10 yr AMIP CCM2 simulation. The meridionally symmetric increase in tropical upper tropospheric temperature includes anvil-induced increase in radiative equilibrium T and decreased heat export by the Hadley cell. There is no significant change in tropical atmospheric stability beneath 200 mb.

3.3. Radiative Forcing

We present the radiative results of the experiment in terms of top-of-atmosphere (TOA) cloud forcing, observed by the Earth Radiation Budget Experiment (ERBE) satellite system from 1985–1989 [*Hurrell and Campbell, 1992*]. Shortwave cloud forcing (SWCF) is defined as the net increase in reflected shortwave (SW) flux at TOA due to cloud scattering and absorption. Figure 8 shows zonal average SWCF for January and July. Dramatic changes seen in condensate distribution and phase (Figures 4 and 5), are not seen in zonal

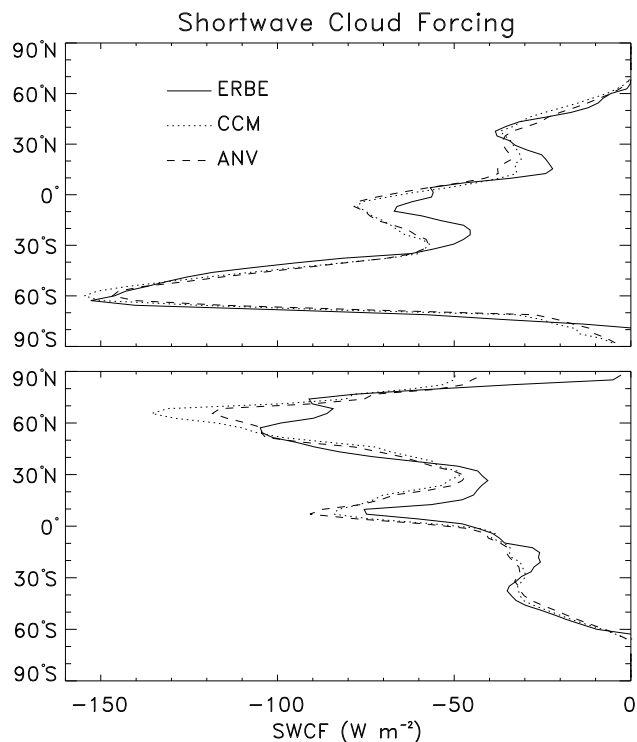


Figure 8. Zonal average shortwave cloud forcing SWCF (W m^{-2}) from ERBE (solid), CCM (dotted), and ANV (dashed) for (a) January and (b) July.

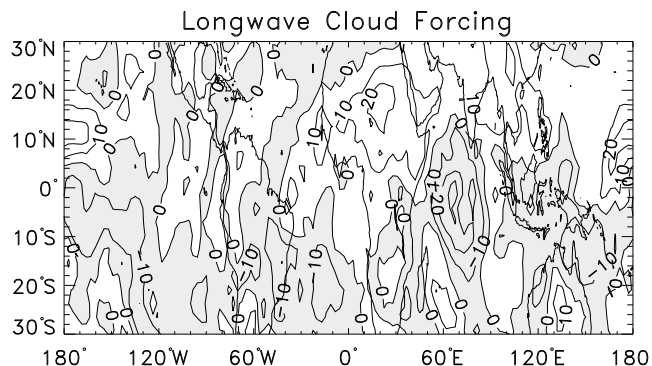


Figure 9. As in Figure 5 but for longwave cloud forcing LWCF (W m^{-2}). Contour interval is 10 W m^{-2} .

average cloud forcing. The models predict similar equatorial LWP beneath 600 mb but ANV has up to 5 times more equatorial IWP. Agreement in modeled tropical cloud forcing illustrates how increased IWP can radiatively offset increased r_e (Section 2.2). ANV worsens the zonal average bias at the July ITCZ by improving (increasing) SWCF in the equatorial east Pacific and Atlantic oceans without reducing SWCF in the Indo-Pacific.

The effect of cloud on terrestrial or longwave (LW) radiation, that is, the reduction in outgoing longwave radiation (OLR) due to cloud condensate, is called longwave cloud forcing (LWCF). LWCF is a radiative proxy for tropical anvil. Figure 9 shows the geographic variation of change in January tropical LWCF due to convectively generated anvils. July results (not shown) confirm LWCF generally increased in the winter hemisphere and decreased in the summer. The strongest bias of the ANV prognostic anvil scheme is an overestimate of cloud forcing over wintertime desert, due to weak sublimation in subsidence regimes. Usually enhanced ice amount and fraction in the prognostic anvil balances the weaker mass extinction efficiency of large ice crystals because hydrometeor size is specified to increase with hydrometeor height [Kiehl *et al.*, 1996]. However, LWCF significantly decreases (and improves) over the central Indian Ocean in January despite a ubiquitous increase in anvil mass in the tropics (cf. Figure 5). This is due to reduced upper level divergence over the central Indian Ocean, a region where prognostic anvil significantly alters the vertical distribution of cloud radiative effects.

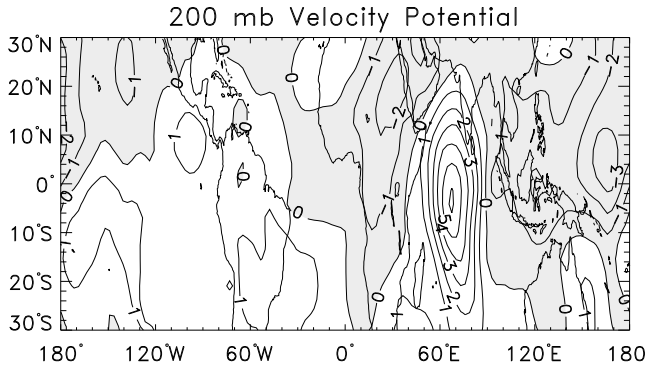


Figure 10. As in Figure 5 but for 200 mb velocity potential χ ($\text{m}^2 \text{s}^{-1}$). Contour interval is $1 \times 10^6 \text{ m}^2 \text{s}^{-1}$. Shading indicates less subsidence (more divergence).

3.4. Tropical Circulation

The change in large scale divergent motion in the tropics due to prognostic anvil representation is shown in Figure 10, which depicts the geographic response of the January 200 mb velocity potential χ . Deep convection shifts toward the winter hemisphere (cf. Figure 6). ECMWF analyses confirm the strong maxima (reduced divergence) over the central Indian Ocean eliminates a persistent convective bias. The decreased Indian Ocean convection also decreased subsidence over African and Arabian desert, allowing too much high cloud to form there (Figure 9).

As seen above, TOA cloud forcing does not reveal the full extent of circulation change due to anvil representation. Tropical circulation is sensitive to the specific vertical (and horizontal) location of anvil heating [Ramaswamy and Ramanathan, 1989; Sherwood *et al.*, 1994]. Figure 11 shows the vertical profile of simulated diabatic heating components over the central Indian Ocean for January conditions. The CCM heating profile, Figure 11a, is typical of deep convective regions in both models. Convective heating dominates radiative from the boundary layer to 250 mb. Large scale heating in the upper troposphere, representing stratiform condensation in anvil, enhances latent heating but the stratiform precipitation evaporatively cools the lower troposphere. SW heating is 30–60% of LW cooling from 800–200 mb, and dominates Q_T from 150–100 mb [Ramaswamy and Ramanathan, 1989].

Differences between ANV and CCM heating profiles, shown in Figure 11b, range from 10–50% of mean heating rates. The prognostic anvil representation reduces anvil formation over the central Indian Ocean. Re-

duced condensate absorptivity increases LW cooling by $\sim 30\%$ from 800–400 mb and enhances anvil-base heating near 300 mb. This radiative heating dipole increases atmospheric stability. Weaker vertical motion and upper level divergence (Figure 10) are accompanied by a large reduction in convective heating and precipitation (3 mm d^{-1}). Reduced convective activity also dries the column, which exacerbates increased cooling beneath 400 mb. Thus, a relatively small reduction in anvil heating appears to leverage much larger reductions in latent heating. This behavior agrees with Sherwood *et al.* [1994], who suggest compensation between vertical motion and anvil heating is an efficient means of restoring energy balance in a regime of weak horizontal gradients of moist static energy. Differences in diabatic heating components are $< .2 \text{ K day}^{-1}$ in July, when much of the central Indian Ocean is colder than 28°C , and the prognostic anvil effect is minimal.

Significant changes in precipitation and high cloud also occur in the tropical Pacific in January. Precipitation associated with the Australian monsoon shifts northward. This shift enhances Micronesian rainfall by up to 7.5 mm d^{-1} , and mid-tropospheric heating rates by up to 2.7 K day^{-1} .

3.5. Extratropical Response

Hoskins and Karoly [1981] showed extratropical stationary wave structure is sensitive to the distribution of tropical diabatic heating. The prognostic representation of tropical anvil significantly alters stationary wave patterns from the central Pacific to western Europe. Figure 12 compares the observed and modeled wintertime 500 mb height field. ANV deepens the central Pacific trough and shifts it $\sim 10^\circ \text{E}$. The associated ridge splits flow around California but reproduces observed ridging over the west coast of Canada, absent in CCM. ANV strengthens the ridge over west Europe, as observed, and shifts the central European trough $\sim 20^\circ \text{E}$ towards analyses. Model differences are 1–3 times model standard deviation in the vicinity of these ridges. These disturbances in extratropical planetary wave structure originate near the tropical Indo-Pacific heating disturbances and propagate to the extratropics. A similar North American response, also linked to a northward shift of Australian monsoon precipitation, occurred in Kiehl [1994].

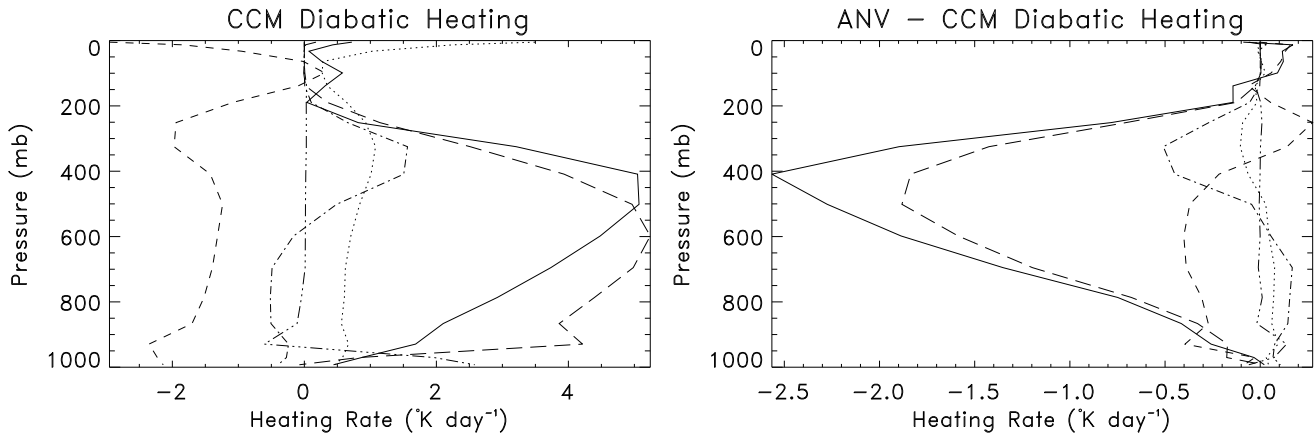


Figure 11. Model simulated profiles of (a) diabatic heating (K day^{-1}), and (b) differences between models (ANV-CCM) for the central Indian Ocean ($15^{\circ}\text{S}-5^{\circ}\text{N}$, $60-80^{\circ}\text{E}$) for 1985-1989 January. Heatings shown are total diabatic (solid), shortwave (dotted), longwave (short dash), resolved (dash-dot), turbulent (dash-dot-dot-dot), and convective (long dash). Note difference in scales.

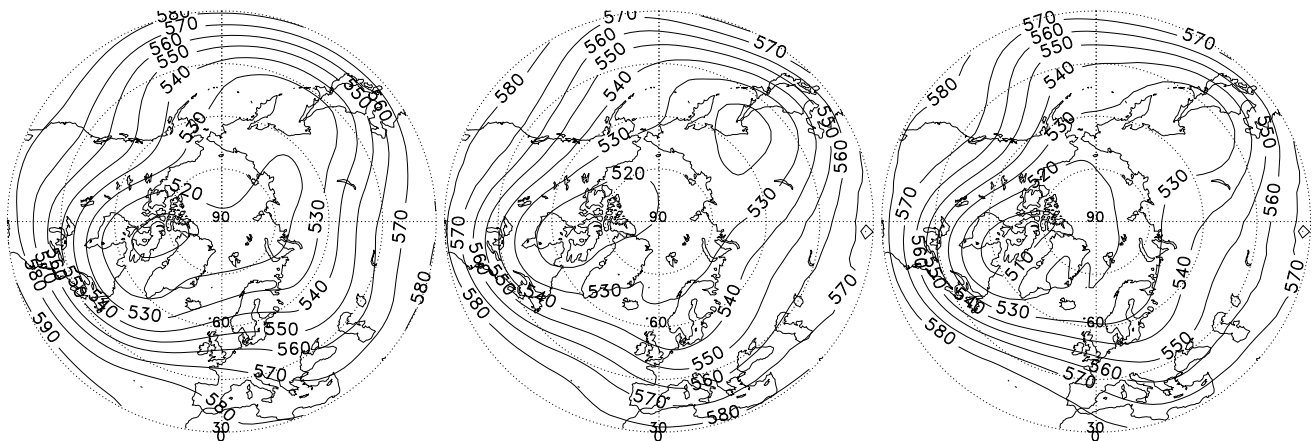


Figure 12. January 500 mb geopotential height field (gpm) for $30-90^{\circ}\text{N}$ from (a) ECMWF 1990-1995 analyses and model simulations of 1985-1989 by (b) CCM and (c) ANV. Contour interval is 10 gpm.

4. Cloud Response to SST Forcing in the Equatorial Pacific

The Equatorial Pacific SST anomaly associated with the 1987 El Niño provides a stringent test of model ability to mimic observed changes in convective patterns and associated anvil cloud. During the 1987 El Niño the center of deep convection, accompanying a large positive SST anomaly, shifted from the west to the central equatorial Pacific. Cloud forcing responded by increasing in the central and east equatorial Pacific through much of 1987, while cooler SST reduced cloud forcing in the west. *Hartmann and Michelsen [1993]* and *Chou [1994]* emphasize cloud enhancement from 10°S – 10°N was largely compensated by clearer sky from 10 – 30° in both hemispheres. We will use the strong SST anomaly in the equatorial Pacific region from 10°S – 10°N to test the deep convective response of the differing anvil representations to transient SST forcing. We focus on Springtime behavior because equatorial SST peaks in April (when the seasonal cycle peaks), and proximity to the equinox maximizes the hemispheric symmetry of solar forcing [*Ramanathan and Collins, 1991*]. The Spring SST of the entire equatorial Pacific (10°S – 10°N , 140°E – 90°W) warmed $.9^{\circ}\text{K}$ from 1985 to 1987, while the central equatorial Pacific alone (10°S – 10°N , 180 – 130°W) warmed 1.2°K . Differencing the cold year (1985) Spring months from the warm (1987) removes the mean cloud forcing state and isolates the cloud forcing sensitivity (which implicitly includes any reorganization of convection patterns) to SST change. Note that atmospheric response could not feed back to SST (a prescribed boundary condition).

Figure 13 shows change in modeled cloud condensate δq_c for 1987–1985 over the equatorial Pacific averaged for Spring. Note δ refers to 1987–1985 temporal change for a given model, not to inter-model change. High cloud increases in both models over the central equatorial Pacific (where δSST peaks) in 1987, and decreases over the western equatorial Pacific. ANV predicts δq_c extrema at the same longitude as CCM (145°E , 175°W), but roughly 100 mb higher, and 2–4 times stronger. Yearly ERBE LWCF (not shown) suggests q_c should increase from 140 – 110°W , as ANV predicts. Thus prognostic anvil representation strengthens and appears to improve CWP response to SST, but this cannot be demonstrated conclusively without reliable observational estimates of CWP.

Figure 14 plots δLWCF vs. δSWCF (i.e., cloud forcing sensitivity to SST) for the equatorial Pacific. Crosses represent GCM gridpoint ($\sim 300^2\text{ km}^2$) monthly aver-

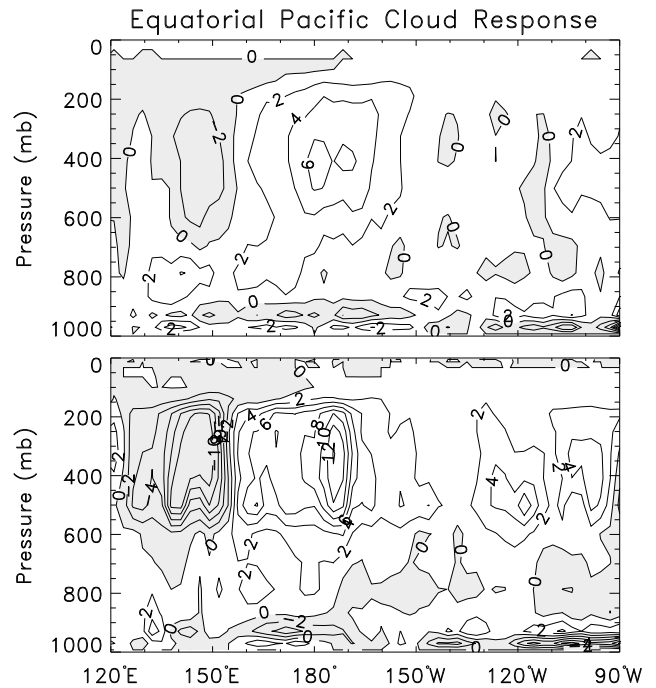


Figure 13. Longitude-height profile of the 1987–1985 difference in Spring quarter (March, April, and May) mean condensate q_c (mg kg^{-1}) over the equatorial Pacific (averaged 10°S – 10°N , ocean only) simulated by (a) CCM and (b) ANV. Contour interval is 2 mg kg^{-1} . Shading indicates q_c decrease from 1985 to 1987.

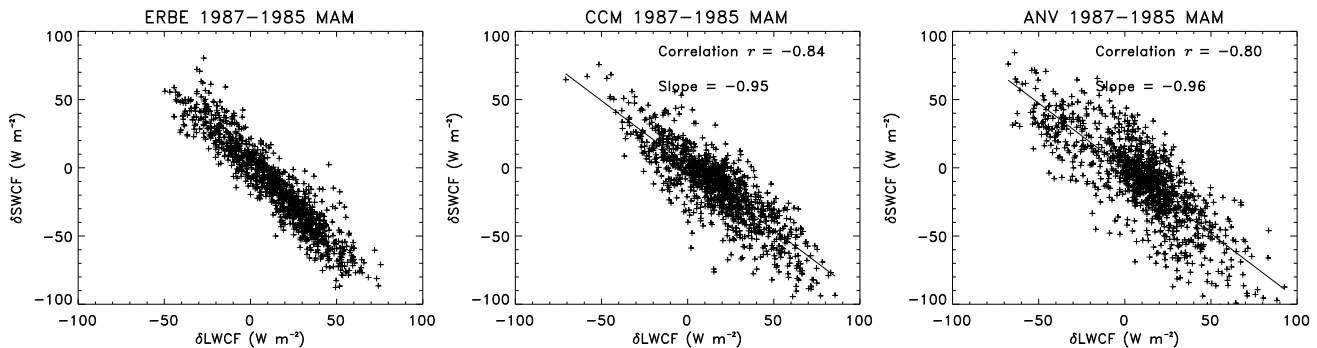


Figure 14. 1987–1985 differences in Spring quarter (March, April, and May) monthly mean maritime LWCF and SWCF (W m^{-2}) over the Equatorial Pacific (10°S – 10°N , 140°E – 90°W) for (a) ERBE, (b) CCM, and (c) ANV. Solid line is least-squares fit.

ages. Note δLWCF is positively correlated with δSST so the upper left of the scattergrams are dominated by points from the equatorial west Pacific, and the center and lower right by points from the central and east equatorial Pacific. Gridpoints with $\delta\text{LWCF} < -20 \text{ W m}^{-2}$ are more copious in ANV, but extend unrealistically beyond $\delta\text{LWCF} < -50 \text{ W m}^{-2}$. This response, and weaker response of the prognostic anvil representation to $\delta\text{SST} \gtrsim 2^{\circ}\text{C}$ ($\delta\text{LWCF} > 50 \text{ W m}^{-2}$), stem from the prognostic formulation of cloud mass. The diagnostic cloud mass, which determines CCM cloud forcing, varies approximately exponentially with SST during convection [Kiehl *et al.*, 1996]. In contrast, ANV cloud mass (hence cloud forcing) peaks with maximum 500 mb convective intensity, which is not necessarily collocated with SST maxima [Hack, 1994]. By decoupling cloud mass from SST, the prognostic anvil representation couples cloud forcing more tightly to other factors determining convective intensity, e.g., atmospheric instability, evaporation, and surface level wind [Fu *et al.*, 1990]. In summary, the prognostic representation of anvil production and structure has generally improved LWCF response for $\delta\text{SST} < 0^{\circ}\text{C}$ and worsened LWCF response for $\delta\text{SST} > 2^{\circ}\text{C}$.

The slope $m \equiv \delta\text{SWCF}/\delta\text{LWCF}$ approximately measures the reduction in surface insolation relative to the increase in atmospheric heating. The ERBE data show local net cloud forcing response to El Niño is a linear ($|r| = .94$), moderately negative feedback ($|m| \approx 1.2$), i.e., the albedo effect of anvil responds more strongly to local SST anomalies than the greenhouse effect. Both models predict $m \approx -.95$, i.e., cloud forcing is a weak positive local feedback to column energy for equatorial Pacific SST change, rather than a moderate neg-

ative feedback, as observed. This model agreement is surprising because Ramanathan and Collins [1991] argue $|m| > 1$ due to radiative properties of tropical anvil, which is diagnosed in CCM, but prognosed by (1) in ANV. Despite model differences in anvil representation, the trends of δLWCF with δSST closely agree with each other and observations: ERBE, CCM, and ANV trends of δLWCF with δSST are 17.0 , 15.7 , and $16.0 \text{ W m}^{-2} \text{ K}^{-1}$, with correlations $.65$, $.60$, and $.54$, respectively. However, ERBE, CCM, and ANV trends of δSWCF with δSST are -20.1 , -12.8 , and $-15.5 \text{ W m}^{-2} \text{ K}^{-1}$, with correlations $-.59$, $-.43$, and $-.44$, respectively. Thus the primary reason both model underestimate $|m|$ is their 25–45% bias in SWCF response.

Ramanathan and Collins [1991], in their Table 1, showed $|m| > 1$ over the equatorial Pacific independent of which non-El Niño season or year is used for δ . Moreover, the same qualitative behavior is ubiquitous over equatorial Pacific subregions (i.e., east, central, west) (not shown). Thus atmospheric GCMs should adequately simulate m in order to realistically cooperate with SST changes when coupled to an oceanic GCM, e.g., in climate change and ENSO experiments. Studies are currently underway at NCAR which should improve cloud radiative response to SST change, i.e., simulation of m . These include representing anvil with fully prognostic microphysical schemes, using probability distributions of tropical cloud fraction determined from satellite observations, and imposing observed hydrometeor effective radius.

5. Conclusions

Radiative forcing from cirrus anvil plays a dominant role in determining the diabatic heating which drives the general circulation yet many features of tropical anvil structure and lifecycle are not represented in current GCM anvil parameterizations. Five year integrations of the National Center for Atmospheric Research Community Climate Model (CCM2) were used to elucidate climate features sensitive to the representation of anvil production and structure. Anvil features emphasized in the sensitivity study included the direct relationship between anvil growth and anvil-base convective mass flux, mesoscale condensate formation, the excess of ice over supercooled liquid, and the vertical distribution of condensate.

The direct effect of improving anvil representation is to sequester more condensate in the upper troposphere, a larger fraction of which is ice. The radiative effects of enhancing ice amount and fraction were approximately balanced by weaker radiative extinction per unit mass because anvil vertical location was tied to larger hydrometeor size. Thus top-of-atmosphere climatological radiative measures such as cloud forcing were not biased by two to fourfold increases in tropical anvil mass. The thermal structure and circulation of the tropics were more dramatically affected due to a vertical shift in heating.

Enhanced anvil perturbs the tropical upper troposphere temperature structure more strongly in winter, when the column is clearer and anvil radiatively heats the troposphere above 200 mb. In the summer tropics, enhanced anvil occurs in a “deep cloud” environment, reducing radiative cooling up to 200 mb, and enhancing cooling above that. Reduced optical depth keeps the intrinsically greater solar absorption of ice relative to liquid from causing a ubiquitous heating increase above 600 mb. Radiative heating contributes to warming the region just below the tropical tropopause 2–3 °K.

Based on the 1987 El Niño, the prognostic anvil formulation improves longwave cloud radiative response to SST cooling but worsens response to warming > 2 °C. The net response of convection is a shift toward the winter hemisphere in solstice months. This convective reorganization reduced Hadley cell strength and eliminated a persistent convective bias the central Indian Ocean. Moreover, the increased convection and high cloud north of the equator in January propagate Rossby waves to the extratropics. This causes significant ridging in the 500 mb height field over the west coasts of North America and Europe, which substantially im-

proves agreement with analysis.

In summary, climate features sensitive to anvil representation include tropical upper troposphere temperature structure, Hadley cell strength, tropical deep convection, and the northern hemisphere wintertime flow field. Many of these responses improved the climate simulation. Thus our study isolates some fundamental climate statistics in the tropics and extratropics that are partially controlled by features of tropical anvil not represented in most current GCM anvil parameterizations. Accounting for these features should be a high priority for future GCM cloud parameterizations.

Acknowledgments. CSZ gratefully acknowledges discussions with B. Briegleb and R. Saravanan. G. Branstator provided insight interpreting Figure 12. P. Rasch provided helpful guidance with cloud parameterization. This work was supported in part by NASA Earth Observing System project W-17,661 and by DOE Atmospheric Radiation Measurements Program grant DE-AI05-92ER61376.

References

- Ackerman, T. P., K.-N. Liou, F. P. J. Valero, and L. Pfister, Heating rates in tropical anvils, *J. Atmos. Sci.*, *45*, 1606–1623, 1988.
- Charlock, T. P., and V. Ramanathan, The albedo field and cloud radiative forcing produced by a general circulation model with internally generated cloud optics, *J. Atmos. Sci.*, *42*, 1408–1429, 1985.
- Chou, M.-D., Coolness in the tropical Pacific during an El Niño episode, *J. Clim.*, *7*, 1684–1692, 1994.
- Del Genio, A. D., M.-S. Yao, W. Kovari, and K. K.-W. Lo, A prognostic cloud water parameterization for global climate models, *J. Clim.*, *9*, 270–304, 1996.
- Donner, L. J., A cumulus parameterization including mass fluxes, vertical momentum dynamics, and mesoscale effects, *J. Atmos. Sci.*, *50*, 889–906, 1993.
- Ebert, E. E., and J. A. Curry, A parameterization of ice cloud optical properties for climate models, *J. Geophys. Res.*, *97*, 3831–3836, 1992.
- Fu, R., A. D. Del Genio, and W. B. Rossow, Behavior of deep convective clouds in the tropical Pacific deduced from IS-CCP radiances, *J. Clim.*, *3*, 1129–1152, 1990.
- Gamache, J. F., and R. A. Houze, Jr., Water budget of a mesoscale convective system in the tropics, *J. Atmos. Sci.*, *40*, 1835–1850, 1983.
- Grabowski, W. W., M. W. Moncrieff, and J. T. Kiehl, Long-term behavior of precipitating tropical cloud systems: A numerical study, *Q. J. R. Meteorol. Soc.*, *122*, 1019–1042, 1996.
- Gregory, D., and D. Morris, The sensitivity of climate simulations to the specification of mixed phase clouds, *Clim. Dyn.*, *12*, 641–651, 1996.

- Hack, J. J., Parameterization of moist convection in the National Center for Atmospheric Research community climate model (CCM2), *J. Geophys. Res.*, *99*, 5551–5568, 1994.
- Hartmann, D. L., and M. L. Michelsen, Large-scale effects on the regulation of tropical sea surface temperature, *J. Clim.*, *6*, 2049–2062, 1993.
- Hoskins, B. J., and D. J. Karoly, The steady linear response of a spherical atmosphere to thermal and orographic forcing, *J. Atmos. Sci.*, *38*, 1179–1196, 1981.
- Houze, R. A., Jr., Observed structure of mesoscale convective systems and implications for large-scale heating, *Q. J. R. Meteorol. Soc.*, *115*, 425–461, 1989.
- Hurrell, J. W., and G. G. Campbell, *Monthly Mean Global Satellite Data Sets Available in CCM History Tape Format*, NCAR Tech. Note NCAR/TN-371+STR, National Center for Atmospheric Research, Boulder, Colo., 1992, nTIS PB92-186121.
- Kiehl, J. T., Sensitivity of the simulated climate to cloud effective drop size specification, *J. Geophys. Res.*, *99*, 23107–23115, 1994.
- Kiehl, J. T., B. A. Boville, B. P. Briegleb, J. J. Hack, P. J. Rasch, and D. L. Williamson, Description of NCAR community climate model (CCM3), *Tech. Rep. NCAR/TN-420+STR*, National Center for Atmospheric Research, Boulder, Colo., 1996.
- Leary, C. A., and R. A. Houze, Jr., The contribution of mesoscale motions to the mass and heat fluxes of an intense tropical convective system, *J. Atmos. Sci.*, *37*, 784–796, 1980.
- Lohmann, U., and E. Roeckner, Influence of cirrus cloud radiative forcing on climate and climate sensitivity in a general circulation model, *J. Geophys. Res.*, *100*, 16305–16323, 1995.
- Machado, L. A. T., and W. B. Rossow, Structural characteristics and radiative properties of tropical cloud clusters, *Mon. Weather Rev.*, *121*, 3234–3260, 1993.
- Mapes, B. E., and R. A. Houze, Jr., Cloud clusters and superclusters over the oceanic warm pool, *Mon. Weather Rev.*, *121*, 1398–1415, 1993.
- McFarquhar, G. M., and A. J. Heymsfield, Microphysical characteristics of three anvils sampled during the Central Equatorial Pacific Experiment, *J. Atmos. Sci.*, *53*, 2401–2423, 1996.
- McFarquhar, G. M., and A. J. Heymsfield, Parameterization of tropical cirrus ice crystal size distributions and implications for radiative transfer: Results from CEPEX, *J. Atmos. Sci.*, 1997, in Press.
- Ramanathan, V., and W. Collins, Thermodynamic regulation of ocean warming by cirrus clouds deduced from observations of the 1987 El Niño, *Nature*, *351*, 27–32, 1991.
- Ramanathan, V., E. J. Pitcher, R. C. Malone, and M. L. Blackmon, The response of a spectral general circulation model to refinements in radiative processes, *J. Atmos. Sci.*, *40*, 605–630, 1983.
- Ramaswamy, V., and V. Ramanathan, Solar absorption by cirrus clouds and the maintenance of the tropical upper troposphere thermal structure, *J. Atmos. Sci.*, *46*, 2293–2310, 1989.
- Senior, C. A., and J. F. B. Mitchell, Carbon dioxide and climate: The impact of cloud parameterization, *J. Clim.*, *6*, 393–418, 1993.
- Sherwood, S. C., V. Ramanathan, T. P. Barnett, M. K. Tyree, and E. Roeckner, Response of an atmospheric general circulation model to radiative forcing of tropical clouds, *J. Geophys. Res.*, *99*, 20829–20845, 1994.
- Slingo, A., A GCM parameterization for the shortwave radiative properties of water clouds, *J. Atmos. Sci.*, *46*, 1419–1427, 1989.
- Slingo, A., and J. M. Slingo, The response of a general circulation model to cloud longwave radiative forcing. I: Introduction and initial experiments, *Q. J. R. Meteorol. Soc.*, *114*, 1027–1062, 1988.
- Sui, C. H., K. M. Lau, W. K. Tao, and J. Simpson, The tropical water and energy cycles in a cumulus ensemble model. Part I: Equilibrium climate, *J. Atmos. Sci.*, *51*, 711–728, 1994.
- Tiedtke, M., Representation of clouds in large-scale models, *Mon. Weather Rev.*, *121*, 3040–3061, 1993.
- Webster, P. J., and G. L. Stephens, Tropical upper-tropospheric extended clouds: Inferences from winter MONEX, *J. Atmos. Sci.*, *37*, 1521–1541, 1980.
- Williamson, D. L., and P. J. Rasch, Water vapor transport in the NCAR CCM2, *Tellus*, *46A*, 34–51, 1994.
- Wong, T., G. L. Stephens, W. Paul Stackhouse, Jr., and F. P. J. Valero, The radiative budgets of a tropical mesoscale convective system during the EMEX-STEP-AMEX experiment 1. Observations, *J. Geophys. Res.*, *98*, 8683–8693, 1993a.
- Wong, T., G. L. Stephens, W. Paul Stackhouse, Jr., and F. P. J. Valero, The radiative budgets of a tropical mesoscale convective system during the EMEX-STEP-AMEX experiment 2. Model results, *J. Geophys. Res.*, *98*, 8695–8711, 1993b.
- Xu, K.-M., and S. K. Krueger, Evaluation of cloudiness parameterizations using a cumulus ensemble model, *Mon. Weather Rev.*, *119*, 342–367, 1991.
- Zender, C. S., and J. T. Kiehl, Radiative sensitivities of tropical anvils to small ice crystals, *J. Geophys. Res.*, *99*, 25869–25880, 1994.
- J. T. Kiehl and Charles S. Zender, National Center for Atmospheric Research, P.O. Box 3000, Boulder, CO 80307-3000. (e-mail: jtkon@ncar.ucar.edu; zender@ncar.ucar.edu)

Received December 19, 1996; revised May 5, 1997; accepted July 12, 1997.

This preprint was prepared with AGU's L^AT_EX macros v5.01, with the extension package 'AGU++' by P. W. Daly, version 1.6b from 1999/08/19.